RESEARCH ARTICLE

The spectral signature of wind turbine wake meandering: a wind tunnel and field-scale study

Michael Heisel*[1,2], Jiarong Hong[1,3], and Michele Guala[1,2]

[1] Saint Anthony Falls Laboratory, University of Minnesota, Minneapolis, Minnesota, USA

[2] Department of Civil, Environmental, and Geo- Engineering, University of Minnesota, Minneapolis, Minnesota, USA

[3] Department of Mechanical Engineering, University of Minnesota, Minneapolis, Minnesota, USA

ABSTRACT

Field-scale and wind tunnel experiments were conducted in the $2D$-$6D$ turbine wake region to investigate the effect of geometric and Reynolds number scaling on wake meandering. Five field deployments took place: four in the wake of a single 2.5 MW wind turbine and one at a wind farm with numerous 2 MW turbines. The experiments occurred under near-neutral thermal conditions. Ground-based LiDAR was used to measure wake velocities and a vertical array of met-mounted sonic anemometers were used to characterize inflow conditions. Laboratory tests were carried out in an atmospheric boundary layer wind tunnel for comparison with the field results. Treatment of the low-resolution LiDAR measurements is discussed, including an empirical correction to velocity spectra using co-located LiDAR and sonic anemometer. Spectral analysis on the lab- and utility-scale measurements confirm a meandering frequency that scales with the Strouhal number $St = fD/U$ based on the turbine rotor diameter D. The scaling indicates the importance of the rotor-scaled annular shear layer to the dynamics of meandering at the field scale, which is consistent with findings of previous wind tunnel and computational studies. The field and tunnel spectra also reveal a deficit in large scale turbulent energy, signaling a sheltering effect of the turbine which blocks or deflects the largest flow scales of the incoming flow. Two different mechanisms for wake meandering – large scales of the incoming flow and shear instabilities at relatively smaller scales – are discussed, and inferred to be related to the turbulent kinetic energy excess and deficit observed in the wake velocity spectra.

KEYWORDS

DOI: 10.1002/we

Prepared using weauth.cls

Wind Energ. 2017; **00**:2–32

meander; Strouhal; LiDAR; spectra; instability

DOI: 10.1002/we

Correspondence

*Michael Heisel, Saint Anthony Falls Laboratory, University of Minnesota, 2 Third Ave. SE, Minneapolis, MN 55414.

Email: heise070@umn.edu

Received . . .

1. INTRODUCTION

An ongoing challenge in the field of wind energy and atmospheric sciences is the acquisition of reliable field-scale turbulence measurements. Quantifying wind turbine inflow conditions and wake behavior is an important step to improving turbine performance and control and protecting the turbine from damaging unsteady loads. Until recently, wind measurements in the field were primarily captured with anemometer-mounted meteorological towers (met towers) [1, 2, 3, 4]. The capability of met towers to measure turbine inflow and wake conditions is limited by several factors including permanent locality of measurements at a single coordinate point, maximum vertical position limited by tower height, and cost.

Since the introduction of coherent laser light detection and ranging (LiDAR) devices, wind profiling LiDAR has become increasingly popular for both nacelle-mounted [5, 6, 7, 8] and ground-based remote sensing [9, 10, 11, 12, 13, 14]. LiDAR technology represents the best alternative to met towers for wind field experimentation and monitoring with the exception of snow particle velocimetry measurements which provide high resolution spatio(2D)-temporal(1D) flow fields in the turbine wake at field scale [15, 16]. While commercially-available LiDAR has been accepted as means for measuring first-order statistics, inherent limitations of the technology, namely low temporal and spatial resolution, lead to unreliable turbulence measurements [17, 18, 19, 20]. As a result, turbulent statistics derived from LiDAR measurements have been supplemented by, and verified against, high-frequency point measurements such as met-mounted sonic anemometry.

In particular, the use of ground-based wind profiling LiDAR to capture field-scale wake turbulence measurements is key for the study of wake meandering, a relatively large scale and slow oscillation of the wake that does not necessarily require high temporal resolution. The turbine wake meandering pattern is particularly important in wind farms where the wake of a turbine becomes the inflow condition for the immediate downstream unit, affecting the power performance of and loading forces on the downstream turbine. Despite vigorous ongoing research on turbine wake meandering (see [21, 22, 23, 24, 25, 26, 27, 28], among others), the characteristics and the underlying mechanism of this phenomenon are

still not fully understood. So far, two mechanisms have been proposed. The first explanation follows the assumptions of [24] which considers meandering, denoted as dynamic wake meandering, to be primarily driven by large scale turbulence of the incoming boundary layer flow. A model to predict the meandering wake position in time using the inflow wind direction [24] has been verified against field measurements [29, 30]. In the cited studies, 1D and 2D nacelle-mounted LiDAR field measurements were used to identify the wake deficit region and compare the transverse position of the deficit in time with the wake position predicted by the model.

The second explanation for wake meandering is that periodic wake motions result from the instability of the turbine rotor's annular shear layer. The rotor scale argument is consistent with results from wind tunnel experiments [22, 31, 32, 33] and computational models [34, 35], but there is a lack of utility-scale data to support these findings. Experiments with turbine models have shown two-dimensional oscillations of the wake center position, defined by the minimum streamwise velocity, as a function of the downstream distance both in the wall-parallel plane [33] and wall-normal plane [27]. Studies have also used streamwise or spanwise velocity spectra to identify a specific frequency peak or range denoting excess turbulent kinetic energy associated with meandering wake oscillations. The studies have consistently identified meandering wake oscillations occurring in the Strouhal number range St =0.2–0.4 [22, 31, 32, 27, 33] where $St = fD/U$ is the dimensionless number for bluff body flow oscillations. In the given Strouhal number definition, f is the wake meandering frequency, D is the turbine rotor diameter, and U is the mean incoming flow velocity.

The main purpose of this work is to quantify the wake meandering frequency under field and laboratory scale conditions. Reported here are findings from field measurements, captured by ground-based LiDAR in the wake of two different utility-scale wind turbines, and from wind tunnel hotwire measurements in the wake of a miniature turbine model. Based on the findings and results of previous literature, we propose a two-pronged phenomenology for wake meandering that considers both rationales (or mechanisms) described above.

All wake measurements have been taken at different downwind distances from the rotor plane, covering a range between $2D$ and $6D$ where the meandering oscillation is expected to develop at the laboratory scale [33, 34]. The LiDAR data in the Eolos Wind Research field station are complemented by measurements of free-stream conditions captured by sonic anemometers mounted to a met tower. The sonic and LiDAR measurements are also used under undisturbed inflow conditions to develop an empirical correction against contamination in LiDAR turbulence measurements. In the Eolos site, the upwind inflow conditions resemble the canonical rough wall boundary layer [15]. The LiDAR measurements in the second field location are inferred to be representative of a wind power plant, with inflow conditions potentially affected by upwind turbine wake meandering. In this respect, the current investigation aims at identifying the intensity and

DOI: 10.1002/we

periodicity of wake meandering under a range of inflow conditions, operating turbine regimes, and weak thermal stability conditions and compare them with literature results. In Section 2, the field experiment is detailed, including descriptions of the research facility, the WindCube wind profiling LiDAR, and the atmospheric conditions during data acquisition. Results of the experiments are then presented in Sections 3 and 4. A phenomenological interpretation of the results is discussed in Section 5. Appendix A provides an overview of corresponding wind tunnel measurements and Appendix B includes the methodology for an empirical correction to LiDAR velocity spectra.

2. FIELD MEASUREMENTS

2.1. Field sites

Four of the five field deployments in the current study were conducted at the Eolos Wind Research Station in the University of Minnesota Outreach, Research, and Education Park in Rosemount, Minnesota [3, 14, 16]. The site topography is characterized by farmland with small local elevation changes (1–3 m) and sparse trees. The station includes a 2.5 MW Clipper Liberty C96 wind turbine and a meteorological tower 170 m due south of the turbine. The turbine has a hub height $z_{hub} = 80$ m, rotor diameter $D = 96$ m, rated wind speed 11 $\mathrm{m\,s^{-1}}$, and approximate optimal tip-speed ratio $\lambda = 8.5$. Turbine performance data including blade pitch and generated power are continuously captured and stored on local servers.

The 130 m tall met tower has four CSAT3 sonic anemometers located at heights $z = 10$ m, 30 m, 80 m, and 130 m. The anemometers measure velocity in the north-south, east-west, and vertical directions as well as temperature at 20 Hz. The anemometer at $z = 10$ m is used for boundary layer parameterization and thermal stability monitoring, while the anemometers at heights $z = 30$ m, 80 m, and 130 m approximately correspond to the turbine bottom tip, hub, and top tip heights, respectively. Figure 1 shows a schematic of the research site. For further details on the Eolos turbine and met tower, see Chamorro et al. [3].

The other field deployment was conducted at the Xcel Energy Pleasant Valley Wind Farm, a wind farm with one hundred 2 MW turbines scattered across farmland in southern Minnesota [36]. The turbine-turbine spacing throughout the site is non-uniform due to access restrictions imposed by the existing farmland and electric infrastructure. The topography local to the deployment position is similar to the Eolos site. The Pleasant Valley wind turbines are Vestas model V100-2MW with hub height $z_{hub} = 100$ m, rotor diameter $D = 100$ m, and rated wind speed between 6–10 $\mathrm{m\,s^{-1}}$ [37]. The turbines record performance parameters and inflow wind conditions measured by a nacelle-mounted anemometer and store the data as averages over 10-minute windows.

DOI: 10.1002/we

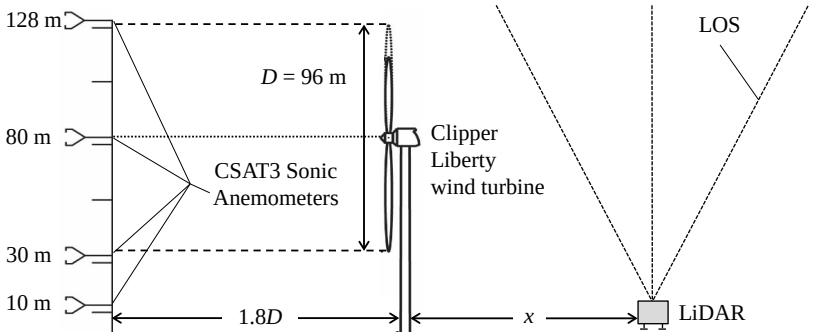

Figure 1. Schematic of the met tower, turbine, and WindCube LiDAR at the Eolos research facility, adapted from Chamorro et al. [3].

2.1.1. Turbine operation

The Eolos turbine has a 1° blade pitch angle in the optimal operating regime, which is characterized by a specific tip speed ratio $\lambda = 8.5$ and power coefficient $C_p = 0.48$. When the turbine performance is derated or the power limit is reached during sustained gust events or a strong mean wind, the blades are pitched out of the wind (i.e. the pitch angle is increased) to maintain a power output below the limit. As a result of the blade pitching, the power coefficient and tip-speed ratio are both reduced and the mean velocity deficit decreases. Note that the intensity of tip vortices, described by their circulation, is proportional to the blade lift and turbine power such that the vortex intensity decreases along with the velocity deficit under reduced power output [38] (see also [16] for estimates of tip vortex circulation). The Pleasant Valley wind turbines operate under a similar principle, but the exact control strategy is not known. It is thus reasonable to expect the annular shear layer, delimiting the wake region and contributing to the meandering instability, to vary in intensity depending on the turbine operating condition and result in a corresponding strong or weak meandering oscillation. The effect of derating on the turbine wake is discussed further in Section 4.2.

2.1.2. Meteorological conditions

For each deployment at the Eolos research station, met tower measurements were used to estimate the thermal stability with both the Monin-Obukhov ratio ζ and the bulk Richardson number Ri_B. The Monin-Obukhov ratio $\zeta = z/L$ was estimated with sonic anemometer values at $z = 10$ m and the Obukhov length $L = -u_*^3\overline{\theta_v}/\kappa g\overline{w'\theta_v'}$, where u_* is the shear velocity, $\overline{\theta_v}$ is the average virtual potential temperature, κ is the von Karman constant, g is the gravitational constant, and $\overline{w'\theta_v'}$ is the virtual potential heat flux at the surface. The shear velocity was approximated using the momentum flux as $u_* \approx \sqrt{-\overline{u'w'}}$, and the virtual potential heat flux was taken as the turbulent heat flux $\overline{w'T'}$. While fluxes were estimated using 20 Hz data, the average virtual potential temperature $\overline{\theta_v}$ was calculated using 1 Hz temperature, pressure, and relative humidity measurements at $z = 10$ m. The bulk Richardson number was calculated as $Ri_B = g\Delta T\Delta z/T(\Delta U^2 + \Delta V^2)$,

DOI: 10.1002/we

Prepared using weauth.cls

where T is the mean temperature in Kelvin, U and V are the mean horizontal velocity components, and gradients were estimated using measurements at $z = 10$ m and 80 m, e.g. $\Delta T \approx T(z = 80\ \mathrm{m}) - T(z = 10\ \mathrm{m})$. The stability parameter values for the deployments are presented and discussed in Section 2.3.

2.2. WindCube LiDAR

A Leosphere WindCube V1 wind profiling LiDAR was used to measure velocities in the wake of the turbine. The pulsed LiDAR measurements were taken at ten custom-defined altitudes ranging from 40 m to 160 m. The WindCube estimates the radial velocity along four line-of-sight (LOS) measurements angled $\phi = 27.83^\circ$ from vertical. The north, east, south, and west LOS (denoted with the subscripts $_N$, $_E$, $_S$ and $_W$), are orientated in the horizontal plane at $\theta = 0^\circ$, 90°, 180°, and 270°, respectively. The LiDAR captures a LOS measurement and rotates to the next azimuth position with a 0.9 Hz approximate sampling frequency. The radial velocity, denoted by Leosphere as the radial wind speed (RWS), is related to the standard velocity components through the equation $RWS_i = u\cos\theta_i\sin\phi + v\sin\theta_i\sin\phi + w\cos\phi$, where $_i$ indicates the LOS direction subscript. The four most recent RWS_i values are used to determine the three spatially-averaged velocity components [17]. The circular horizontal area of the sampling volume is dependent on the altitude z through the equation $A = \pi(z\tan\phi)^2$. The effective height of the sample volume, based on the range-gating and weighting technique of the WindCube, is approximately 16 m independent of altitude [39].

2.2.1. Velocity calculations in local orientation

Issues arising from the large horizontal sampling area can be partially mitigated by positioning the LiDAR in "local" orientation [14]. Rather than positioning the WindCube in alignment with global coordinates, i.e. having the north LOS oriented with true north, the WindCube was oriented such that the north and south LOS were aligned with the anticipated mean wind direction. The streamwise velocity in local orientation then relies on only two LOS measurements:

$$u = \frac{RWS_N - RWS_S}{2\sin\phi}. \tag{1}$$

To account for the time discrepancy between RWS_N and RWS_S measurements, the two series were resampled by linear interpolation to an equivalent time series (using the sampling frequency 0.44 Hz between two LOS measurements). The local orientation has two major advantages: (i) the velocity measurements are more reliable due to a reduction in sample volume, lack of averaging across four radial velocities, and higher correlation of radial velocities when aligned with the mean wind; (ii) the measurements are more likely to remain in the wake under small changes in wind direction (e.g. $\pm 10^\circ$ at $x = 5D$). One disadvantage of local orientation is that the spanwise velocity v is less reliable: the east

DOI: 10.1002/we

and west LOS radial velocities are less correlated, especially in instances when one LOS is in the turbine wake and the other is not. For this reason, the study only considers the streamwise velocity component calculated from the LiDAR measurements.

In local orientation, the north LOS is nearer the turbine than the south LOS. For the Eolos turbine, the hub-height measurement point for each LOS is approximately 42 m ($0.44D$) from the WindCube in the horizontal plane. The wake distance reported in later results is given by the WindCube location and not the LOS measurement points. While local orientation does partially mitigate certain LiDAR limitations, the assumption of spatial homogeneity in the streamwise direction remains.

2.2.2. Measurement resolution

For the WindCube, the general assumption of homogeneity within the sampling volume leads to the specific assumption that velocity fluctuations from the mean are the same at different LOS's, e.g. $u'_N = u'_S$. The assumption is true at the largest scales of turbulence for which the LiDAR sample volume is essentially reduced to a single point [17], but is violated at smaller scales where the non-locality of the LOS radial velocities result in a general overestimation of velocity variance [19]. The variance estimates must therefore be taken with caution. To quantify the resolution limits of the WindCube, it is assumed the smallest time scale the WindCube can resolve is given by $f_{max}(z) = U(z)/d(z)$ where $d(z) = 2z\tan\phi$ is the distance between LiDAR LOS measurement points at a given altitude. The assumption uses Taylor's frozen turbulence hypothesis and the idea that the LiDAR can resolve length scales larger than the sample volume, i.e. the LOS measurement separation $d(z)$. At the Eolos turbine hub height, the maximum frequency is $f_{max} = U_{hub}/84$. Based on this maximum frequency and the turbine rotor diameter, the WindCube can resolve turbulent motions corresponding to $St < 1.1$. Therefore, it is expected the WindCube is able to capture the wake meandering phenomenon which occurs in the Strouhal number range $St = 0.2$–0.4.

Extending the resolution limitations to spectra, velocity spectra estimated using LiDAR are generally accurate for low frequencies representing the largest scales, but energy in the inertial sub-range is overestimated due to the above assumption regarding LOS fluctuations [19]. The resulting spectral shape has been reported in [40, 17]. The spectral error can be avoided by conducting spectral analysis on the radial velocities directly. However, the LOS elevation angle ($\phi = 28^\circ$ from vertical) results in radial velocities primarily dictated by the vertical velocity component, whereas wake meandering predominantly occurs in the horizontal (streamwise and spanwise) plane for wall-bounded flows. To identify the wake meandering signature in the field measurements, it is therefore necessary to use the spatially-averaged streamwise velocity and properly account for the error. To this end, an empirical correction was developed for the WindCube wake data in

DOI: 10.1002/we

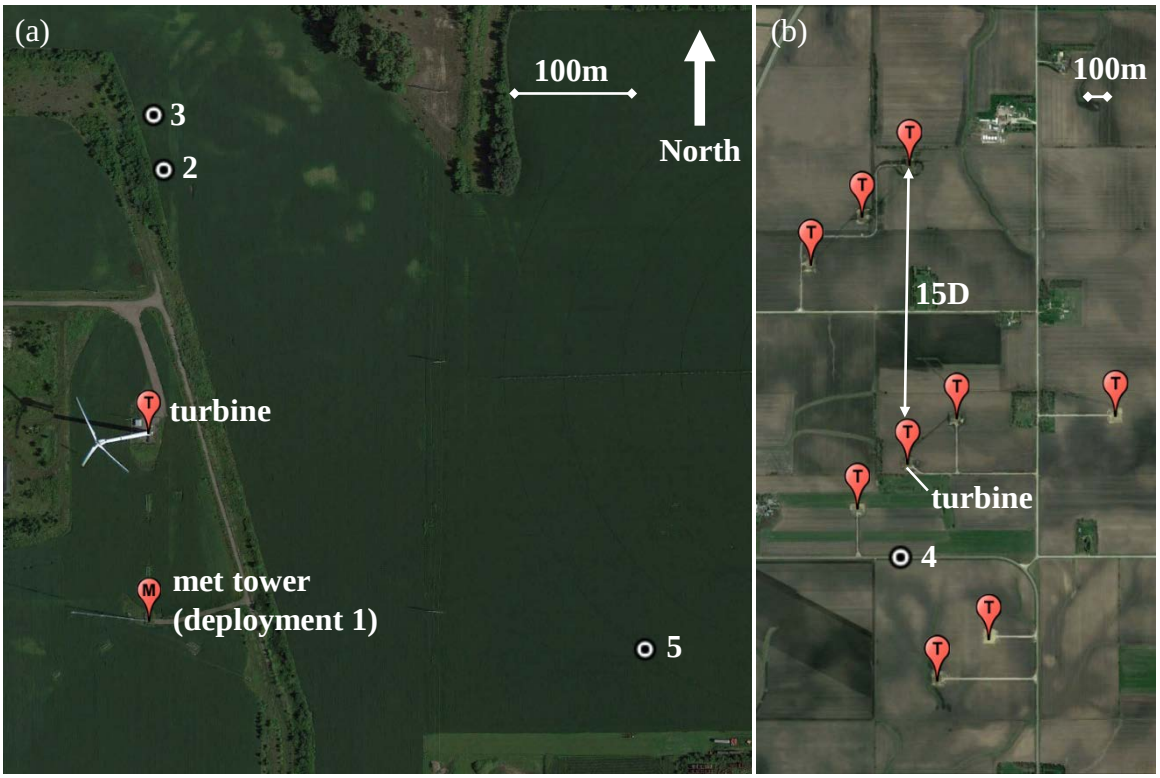

Figure 2. Google Earth satellite photos of the (a) Eolos and (b) Pleasant Valley field deployment sites. The numbered placemarkers indicate wake deployment positions corresponding to the field deployments in Table 1. Met tower data during a period of northerly winds were used for deployment 1.

this study to compensate for the overestimation. The spectral error was approximated with co-located sonic and LiDAR measurements under the same undisturbed inflow condition (see the appended material for the correction methodology).

2.3. Deployments

The five deployments are numbered sequentially in order of downstream distance, and hereon are designated by the deployment number. Figure 2 shows a plan view of the two field sites including the position of the WindCube for each deployment.

For the deployments using the WindCube, the anticipated mean wind direction was determined from weather forecasts and near-real-time wind data available from Eolos servers. The GPS location of the WindCube (shown in Figure 2) was then calculated based on the desired downstream distance and the required bearing to align with the mean wind. Once at the GPS location, the WindCube was oriented with the mean wind and turbine bearing to achieve local orientation as discussed in Section 2.2.1. Wake measurements were captured for periods ranging from 1 to 4 hours.

DOI: 10.1002/we

Table I. Overview of meteorological and turbine conditions for field deployment wake measurements. Values given are averages for the deployment period listed. Wake measurements were captured with LiDAR, except for deployment 1 whose wake data were captured by met tower sonic anemometers. Deployments took place at the Eolos wind research station, except for deployment 4 which took place at the Pleasant Valley wind farm. U_{hub} is the mean inflow wind speed at the turbine hub height.

Deployment	Distance	Date	Start time [CDT]	Duration [hours]	Wind direction [°]	Thermal stability: $\zeta = z/L$	Thermal stability: Ri_B	U_{hub} [m s^{-1}]	C_p	λ	Pitch [°]
1	$1.8D$	2012-07-30	21:34	2.5	356	–	0.14	6.6	0.37	8.6	1.4
2	$2.6D$	2013-10-09	16:14	1	173	-0.05	-0.58	7.3	0.43	8.8	1.2
3	$3.1D$	2013-10-09	14:45	1	179	-0.10	-0.75	7.9	0.40	8.8	1.2
4	$4.8D$	2016-09-28	11:00	4	5	–	–	8.6	0.47	8.4	1.0
5	$5.1D$	2015-10-12	14:53	2.5	290	-0.01	-0.19	14.2	0.19	5.5	9.7

Table I provides an overview of averaged statistics for the field deployments including the downstream distance, the two thermal stability parameters introduced in Section 2.1.2, the inflow wind speed at the turbine hub height U_{hub}, the power coefficient C_p, the tip-speed ratio λ, and the blade pitch angle. The two stability parameters indicate near-neutral conditions for each deployment which, given the high wind speeds, suggests conditions where shear production of turbulence dominated buoyancy effects.

Deployment 1: Deployment 1 is the only case where the WindCube was not employed. For this case study, the met tower was perfectly in the wake of the Eolos turbine and the sonic anemometers were used to describe the wake flow. The observation period was selected from historical met tower data looking for a persistent north wind that would ensure the met tower to be located in the center of the turbine wake. In such a case we are limited by a fixed and close distance to the turbine rotor $x = 1.8D$. This procedure has previously been implemented at the Eolos site to identify the tip vortex spectral signature at the wake edge [41] as opposed to the meandering signature in the wake center. Upwind measurements are not available for this period and the inflow conditions are limited to the turbine nacelle-mounted anemometer. The Monin-Obukhov ratio is not presented for deployment 1 in Table I as the fluxes measured at $z = 10$ m by the met tower are affected by the presence of the turbine. The bulk Richardson number was calculated using the mean temperature and velocity measured at the hub height by turbine nacelle-mounted instruments and the mean temperature measured at $z = 10$ m by the met tower. This approximation uses $U = 0$ at the ground and assumes the temperature at $z = 10$ m is representative of the ground temperature and is unaffected by the turbine in the mean value. The resulting Richardson number $Ri_B = 0.14$

DOI: 10.1002/we

indicates weak thermal stability, consistent with typical stability conditions for the early night deployment time. Based on the turbine performance parameters in Table I, the turbine operated near optimal conditions.

Deployments 2 and 3: Measurements for deployments 2 ($x = 2.6D$) and 3 ($x = 3.1D$) were used in a previous study [14]. The deployments were at the Eolos field site with the WindCube positioned in the turbine wake and the met tower used to characterize inflow conditions (as shown in the Figure 1 schematic). Thermal stability parameters were calculated as discussed in Section 2.1.2 using the met tower inflow measurements at $z = 10$ and 80 m. The thermal stability conditions were weakly unstable. The turbine again operated near optimal conditions.

Deployment 4: For deployment 4 ($x = 4.8D$) the WindCube was positioned in the wake of a turbine at the Pleasant Valley wind farm (i.e. the labeled turbine in Figure 2(b)). The deployment turbine was $15D$ downstream of another turbine in the mean wind direction: the bearing from the upstream turbine to the deployment turbine was 0.5° and the mean wind direction was 5°. The mean hub height wind speed at the upstream turbine was 9.2 $\mathrm{m\,s^{-1}}$and the wind speed at the deployment turbine was 8.6 $\mathrm{m\,s^{-1}}$, suggesting some turbine-turbine interaction. Another turbine was located $10D$ downstream of the deployment turbine in the mean wind direction. The spanwise distance between turbines was 250 m for each of the clusters in Figure 2(b), i.e. the three upstream, three midstream, and two downstream turbines. This distance corresponds to $2.5D$ hub-to-hub separation and $1.5D$ spacing between swept rotor areas. The setting has potential for wind farm effects including upstream wake inflow conditions, spanwise confinement of the wake, and increased aerodynamic roughness. However, the pointwise measurements cannot definitively identify multi-turbine effects besides the apparent velocity deficit discussed above.

The inflow conditions for this deployment are limited to 10-minute windowed average values of the turbine nacelle-mounted anemometers. Neither stability parameter is known for this deployment as surface fluxes are not available to determine the Monin-Obukhov ratio and surface temperature is not available to determine the temperature gradient for the bulk Richardson number. Based on the deployment time and overcast cloud cover, conditions were likely weakly unstable. The turbine operated near optimal conditions.

Deployment 5: Similar to deployments 2 and 3, deployment 5 ($x = 5.1D$) took place at the Eolos field site with the WindCube wake measurements and inflow conditions captured by the met tower. The thermal stability parameters indicate weak instability. The turbine was derated due to the high mean wind speed, with the high pitch angle resulting in the low C_p and λ values shown in Table I.

DOI: 10.1002/we

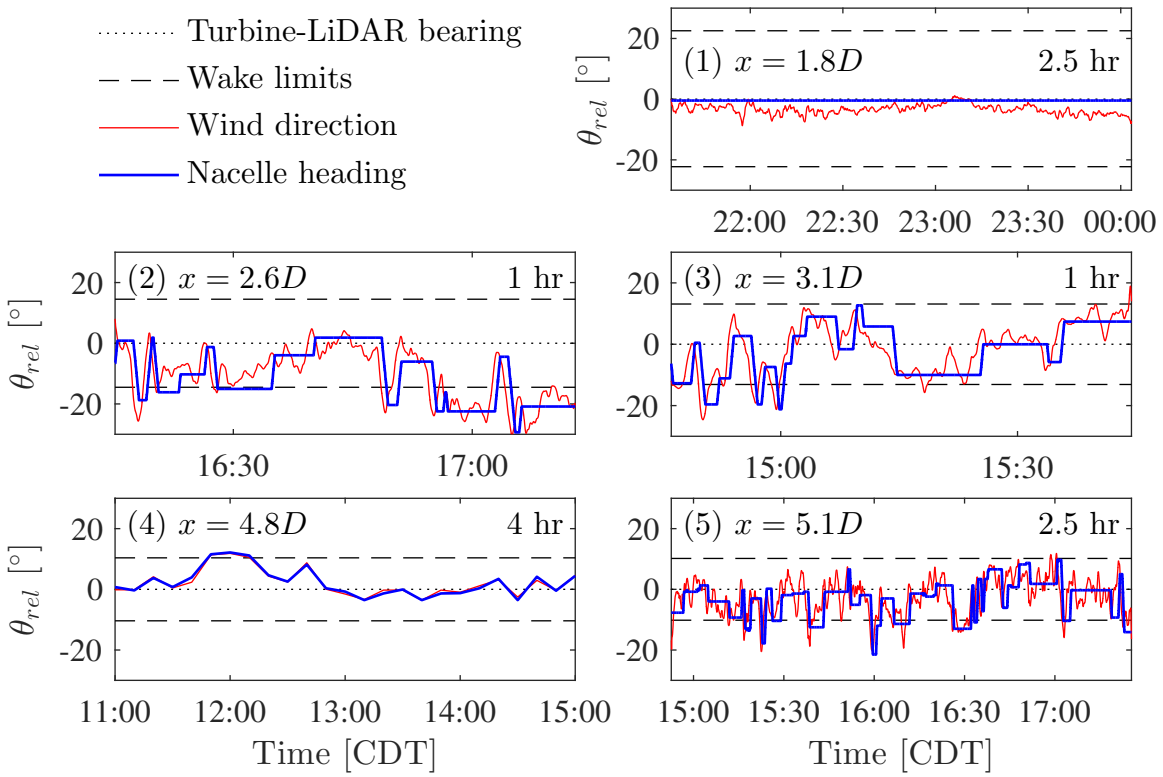

Figure 3. Time series of the wind direction (1-minute average) and turbine nacelle heading relative to the LiDAR position for the five deployments. The wake limits (– –), based on the LiDAR position and an assumed 5° wake expansion angle, represent the direction range for which the LiDAR measurements are in the wake. Numbering (1) through (5) corresponds to the field deployments in Table I. Note that for deployment 4 only 10-minute windowed average direction data were available.

2.3.1. Wind directions

Figure 3 shows the turbine nacelle heading and a 1-minute moving average of the wind direction for each deployment, where the plotted directions are relative to the bearing from the turbine to the wake instrument. The wind direction range for which the WindCube north and south LOS measurements were in the wake of the turbine was estimated based on the LOS geometry and an assumed 5° wake expansion angle. For deployment 1, the limits are based on the met tower location rather than the WindCube LOS. The wake limits consider the wake position to be determined by the wind direction with negligible deflection of the wake under small yaw misalignment [42]. Note that for deployment 4 only 10-minute windowed average direction data were available.

As seen in Figure 3, there were periods with downstream measurements positioned outside of the estimated wake limits. Table II reports the percent of the deployment duration for which the downstream measurements are outside the limits. To assess the effect of out-of-wake measurements on the results, the mean wake deficit for each deployment is calculated using

DOI: 10.1002/we

Table II. Percent of the deployment duration for which the measurements are inside the estimated wake limits due to the wind direction. The effect of non-wake periods is shown by comparing the mean wake deficit $(U_{hub} - U)/U_{hub}$ for all data and for data conditionally sampled to only include periods where the measurements are within the wake limits. The values for deployment 4 are based on low-resolution, 10-minute average wind direction data.

deployment	1	2	3	4	5
data within wake limits (%)	100	67	90	88	88
$(U_{hub} - U)/U_{hub}$ for all data	0.47	0.32	0.24	0.14	0.08
$(U_{hub} - U)/U_{hub}$ for data within wake limits	0.47	0.34	0.24	0.16	0.07

the full time series and a conditionally sampled time series that excludes periods when the measurements are estimated to be out of the wake. Because the overall deficit in Table II is close to the conditionally sampled deficit for each deployment, conditional sampling was not utilized in any further calculations or results.

3. RESULTS: MEAN AND VARIANCE STATISTICS

3.1. Mean velocity profiles

The met tower and turbine nacelle anemometers provide horizontal velocity measurements in the north-south and east-west directions. To compare these inflow measurements with the WindCube velocity measurements, the inflow velocities were rotated into alignment with the WindCube orientation for all results presented in the study. The mean velocity profiles in Figure 4 were determined using the rotated inflow measurements and equation (1) with the WindCube wake measurements. A power law fit of the inflow measurements was used to characterize the boundary layer profile. Deployment 5 has markedly stronger shear under the high wind conditions. The wake deficits for each deployment are listed in Table III. As expected, the wake deficit decreases with increasing downstream distance.

3.2. Velocity variance

One-dimensional velocity spectra were estimated from the WindCube and sonic anemometer streamwise velocities using windowed averaging. To account for slowly varying mean wind conditions, velocity fluctuations were determined from a moving average as $u' = u - \langle u \rangle$ where $\langle u \rangle$ is a 30-minute moving average of the streamwise velocity. Each time series was then segmented into 15-minute windows with 50% overlap and multiplied by a Hanning window to estimate the spectrum

DOI: 10.1002/we

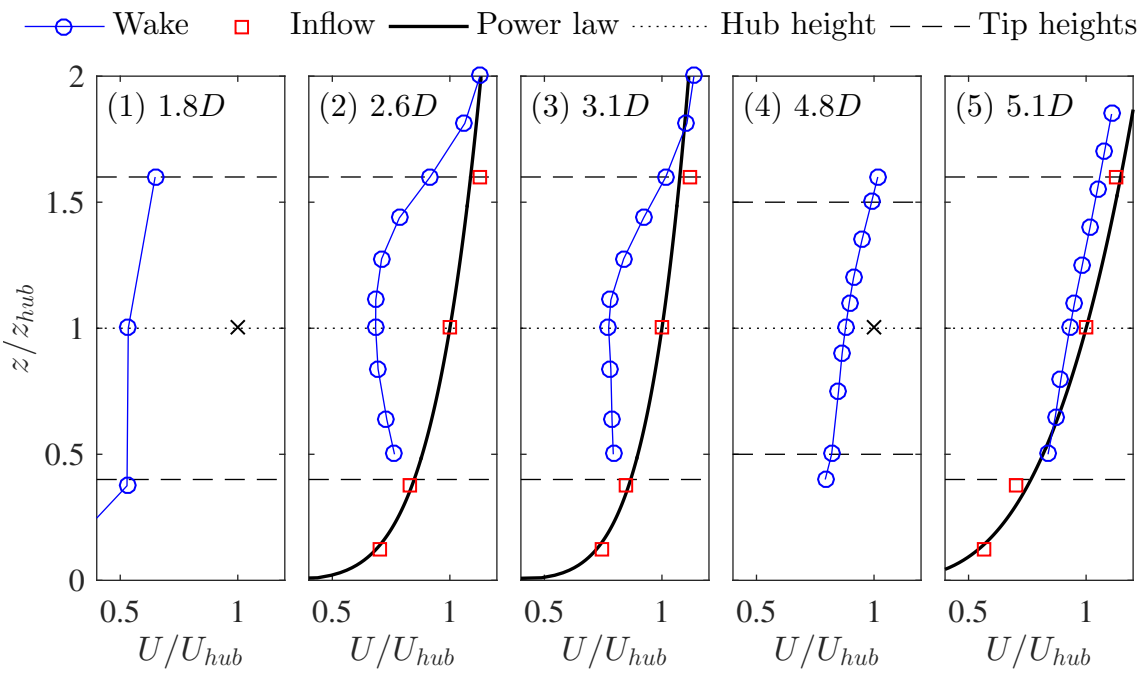

Figure 4. Mean velocity profiles for the five deployments. Numbering (1) through (5) corresponds to the field deployments in Table I. The incoming hub height velocity U_{hub} measured by the turbine nacelle-mounted anemometer ($\times$) is used to normalize deployments without inflow profile measurements. A power law curve $U/U_{hub} = (z/z_{hub})^m$ is fitted to deployments with available inflow profile measurements. Coefficients for the power law curves are $m = 0.18$, 0.16, and 0.29 for deployments 2, 3, and 5, respectively.

Φ_u. As a result, the largest time scale the spectrum can resolve is $f_{min} = 1/15$ min ≈ 0.001 Hz. The velocity variance was estimated as $\sigma_u^2 = \int \Phi_u(f)df$ with the integral limits f_{min} to f_{max}, where f_{max} is the temporal resolution limit of the WindCube as discussed in 2.2.2. The method is analogous to a bandpass filter to ensure the variance is computed using an equivalent range of scales. While the resulting variance values exclude turbulent energy in the smallest and largest scales of the flow, the sonic and WindCube measurements can more reliably be compared. However, the WindCube variance may still be overestimated (see above and [19, 20]). For instance, in the baseline periods where sonic anemometers and LiDAR were co-located (see Appendix B), the estimated variance of the streamwise velocity at hub height range from 0% to 10% higher for the LiDAR than the sonic under various wind and thermal stability conditions.

The root mean square velocity and turbulence intensity for each deployment, from the variance estimate described above, are listed in Table III. Deployment 1 took place at night under slightly stable thermal conditions, resulting in a lower turbulence intensity than the other wake cases despite a nearer downstream position. The highest wake r.m.s. velocity, seen in deployment 5, coincides with the highest inflow mean and r.m.s. velocities. The highest wake turbulence intensity corresponds to the highest C_p (deployment 4).

DOI: 10.1002/we

Table III. Inflow (sonic) and wake (LiDAR) streamwise flow conditions at hub height during the field deployments: σ_u is the root mean square of the streamwise velocity (the turbulence intensity $I = \sigma_u/U_{hub}$ is indicated in parentheses), and $(U_{hub} - U)/U_{hub}$ represents the mean velocity deficit. U_{hub} is the incoming streamwise velocity and U is the wake velocity, both at hub height. Turbulence statistics of the inflow are not available for deployments 1 and 4 due to the low sampling frequency of the nacelle anemometers.

deployment	1	2	3	4	5
inflow σ_u [m s^{-1}] (I)	–	1.10 (0.15)	1.08 (0.14)	–	2.59 (0.18)
wake σ_u [m s^{-1}] (I)	0.97 (0.15)	1.26 (0.17)	1.50 (0.19)	1.69 (0.20)	2.65 (0.19)
$(U_{hub} - U)/U_{hub}$	0.47	0.32	0.24	0.13	0.07

4. RESULTS: SPECTRAL ANALYSIS

In order to interpret wake spectra for utility-scale turbines and compare quantitatively the signature of wake meandering with lab-scale model turbines, new experiments were conducted in a boundary layer wind tunnel. This section includes spectral results of the experiments. For a description of the turbine model and measurements, see Appendix A.

4.1. Wind tunnel spectra

Figure 5 shows wind tunnel results of the streamwise velocity spectra and pre-multiplied spectra at $6D$ downstream of the model turbine for 5 m s^{-1}free stream velocity. The frequency is normalized as the Strouhal number. The inflow spectrum exhibits the theoretical $-5/3$ slope of the inertial sub-range. In Figure 5(b) there is a clear pre-multiplied peak in excess turbulent energy at $St = 0.33$ and the excess energy extends to the smallest measured scales. The same figure also shows a deficit in low frequency energy, which confirms a transfer of turbulent kinetic energy from the very large scales of the incoming flow [43] into the smaller scales in the wake [44]. The shaded area in the pre-multiplied plot is defined by the area under the spectra where the inflow spectrum exceeds the wake spectrum. The St and Φ_u values corresponding to the geometric centroid of the shaded area are taken to represent the central value of the energy deficit. Note that while the pre-multiplied spectrum is useful for visualizing energetic peaks, its area does not represent physically the energy levels. The centroid is therefore calculated from the regular spectrum Φ_u as opposed to $f\Phi_u$, with linear scaling as opposed to logarithmic scaling for both f and Φ.

DOI: 10.1002/we

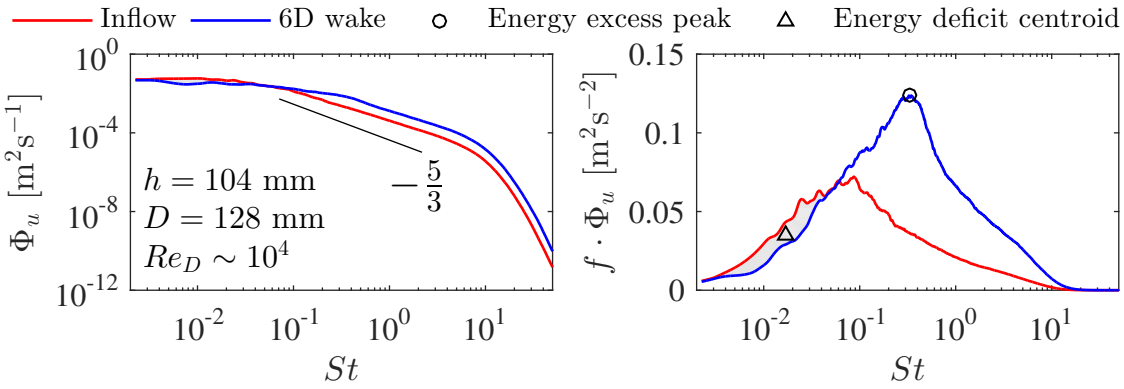

Figure 5. One-dimensional velocity spectra Φ_u (left) and pre-multiplied spectra $f\Phi_u$ (right) for a model turbine wind tunnel experiment. The spectra are estimated from hotwire measurements of the hub height streamwise velocity. The frequency is normalized as the Strouhal number, $St = fD/U_{hub}$. The centroid of large-scale energy deficit (shaded area) is based on the shape of energy deficit in the spectra. For the example case shown, the Strouhal values of the centroid and peak are $St_{centroid} = 0.017$ (△) and $St_{peak} = 0.33$ (○), respectively.

4.2. Field spectra

Field measurement spectra Φ_u were estimated the same as in Section 3.2 except window sizes were reduced to 10 minutes. The shorter windows provide better averaging of the results, and the 10-15 minute time scales contribute less to the wake signature than to the overall variance. For each velocity spectrum using WindCube measurements, the spectral error discussed in Section 2.2.2 is compensated using the correction procedure outlined in Appendix B. Figure 6 shows the corrected pre-multiplied velocity spectra for the five field deployments. The standard deviation of the correction factor is used to represent the correction uncertainty. The deployment 1 inflow spectrum was approximated using met tower data under similar conditions on a separate day. The inflow spectrum is not available for deployment 4 at the Pleasant Valley wind farm.

The energy deficit centroid was calculated in the same manner as for the wind tunnel spectra. For the wind tunnel spectra, as seen in Figure 5, the inflow and wake spectra collapse at the largest scales such that the deficit area is fully resolved. For the field spectra, the collapse is not seen (e.g. deployment 2 in Figure 6) because the spectral window length excludes long time scales which may still exhibit energy deficit in the wake. The deficit centroid defined in the field spectra is therefore skewed towards to a higher St frequency value.

Because the pre-multiplied peaks are less distinct for the field spectra due to limited sample points and natural, uncontrolled inflow conditions, the excess energy centroid was determined for deployments with available inflow spectra. Converse to the energy deficit, the energy excess centroid is based on the area under the spectra where the wake spectrum

DOI: 10.1002/we

exceeds the inflow spectrum. The excess energy centroid is not employed for the wind tunnel spectra because the peak is clearly distinguishable and the extended range of the excess energy towards the smallest scales would skew the centroid to higher, unrepresentative Strouhal number values. For deployment 3, the excess energy shaded area is crescent-shaped for the spectrum Φ_u and the centroid falls outside the area.

The wake spectrum for deployment 1 exhibits a deficit in large scale energy, but no distinct energetic peak in the expected Strouhal range. The identified peak cannot be distinguished from the spectrum noise. The $1.8D$ position may indeed be too near the turbine, before the onset of wake meandering. The laboratory-scale findings of [35, 34, 33] suggest the onset of meandering in the range $2D$–$4D$, corresponding to the interaction between the hub vortex and the shear layer, although such a mechanism may be less relevant for full scale turbines characterized by a rotor diameter much larger than the nacelle diameter. The spectrum in figure 6(1), exhibiting minor differences as compared to the inflow, further indicates that any potentially significant scale-specific turbulent energy added by the turbine nacelle does not exhibit an appreciable signature by $1.8D$.

The difference in general shape of the deployment 1 inflow spectrum in comparison with the other deployments is due to the different stability conditions and lower contribution of large-scale energy for the thermally stable nighttime deployment [45]. The relative deficiency of large scale motions in the incoming flow leads to smaller contributions by the frequency scales $St < 0.1$ to the overall streamwise variance.

Deployments 2 and 3 each demonstrate clear regions of energy deficit and excess in the turbine wake. The difference in inflow and wake spectra extends beyond the standard deviation of the wake correction, indicating the energy deficit and excess are physically robust and outside of the correction uncertainty.

Deployments 4 and 5 occurred at similar downstream positions, but the turbine was performing sub-optimally for deployment 5. While there is no inflow for comparison with the deployment 4 wake spectrum, the pre-multiplied spectrum has a definitive peak and convex shape in the region $St = 0.1$–0.7 that would not manifest under typical turbulent inflow conditions. For deployment 5, there is no region of energy deficit and the excess energy peak cannot be distinguished from the spectrum noise. The lack of a distinct peak for deployment 5 can be interpreted as follows: the low tip-speed ratio and high blade pitch angle result in a weaker, less coherent wake which enables mixing with the surrounding high Re flow. This contributes to a decay in both the velocity deficit and wake meandering signature by $5D$. The interpretation is consistent with the lack of a large-scale energy deficit and the close matching of the wake and inflow spectra assessed for deployment 5. We however recognize that a weaker velocity deficit implies larger convection velocity in the wake and may thus spatially delay the onset of wake meandering to farther downstream positions as has been seen in simulations [46].

DOI: 10.1002/we

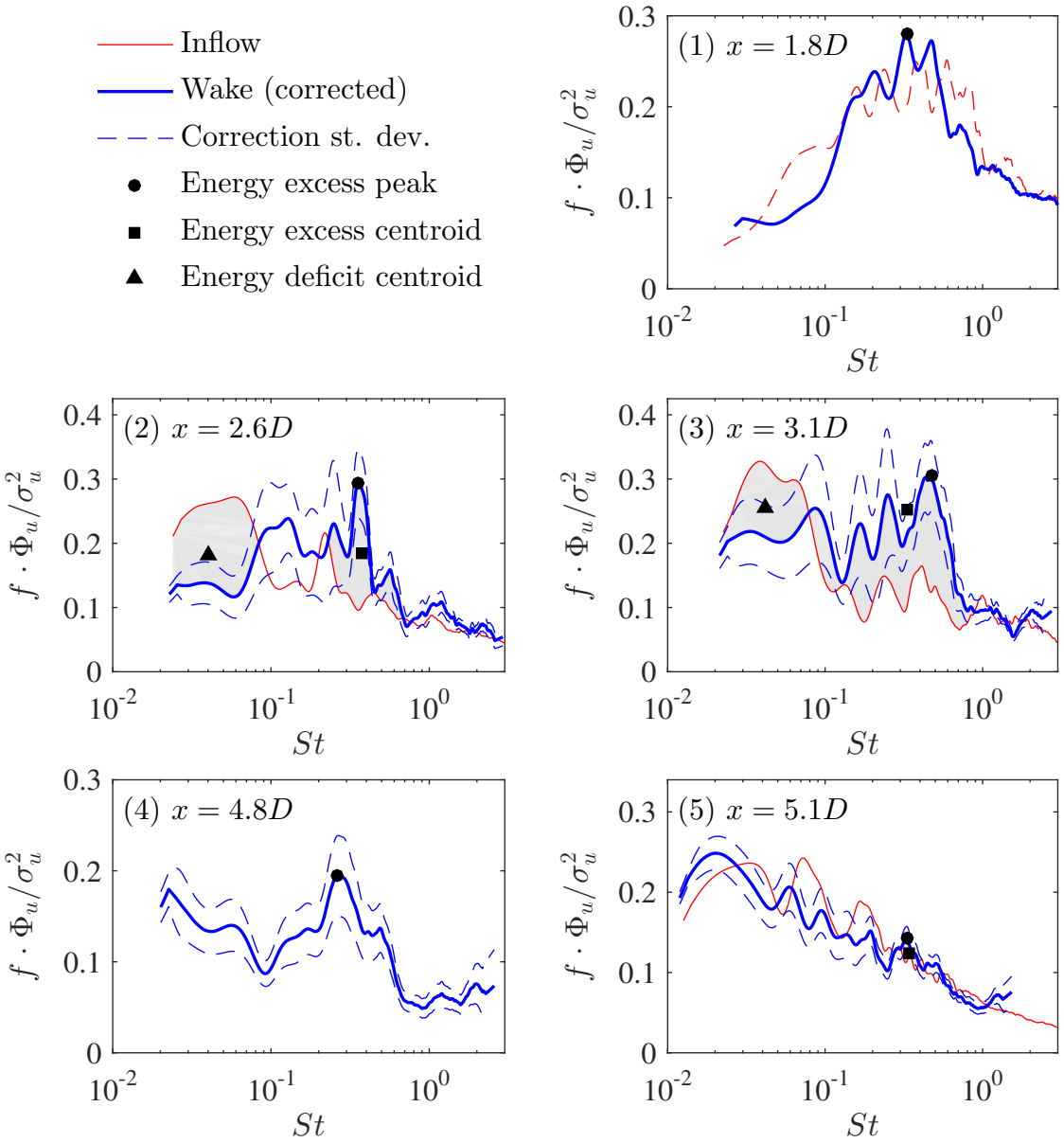

Figure 6. Corrected, pre-multiplied velocity spectra for the five field deployments following Figure 11(d). For deployment 1, the inflow spectrum was approximated using met tower data under similar conditions on separate day. The frequency is normalized as the Strouhal number and the spectra by the variance. The centroid of excess wake energy (shaded area) is based on the shape of excess energy in the spectra, not the pre-multiplied spectra. Numbering (1) through (5) corresponds to the field deployments in Table 1.

In addition to the spectral peak, meandering can be identified visually in the time signal of the wake measurements. Figure 7 shows a sample time signal of the streamwise velocity for the wake measurements in deployment 4. Time is normalized by the period at which the pre-multiplied spectral peak occurs: $T_{peak} = 1/f_{peak} \approx 40$ s. There is a pattern of alternating low and high speed regions passing with a frequency approximately corresponding to T_{peak}. The low-speed

DOI: 10.1002/we

Prepared using weauth.cls

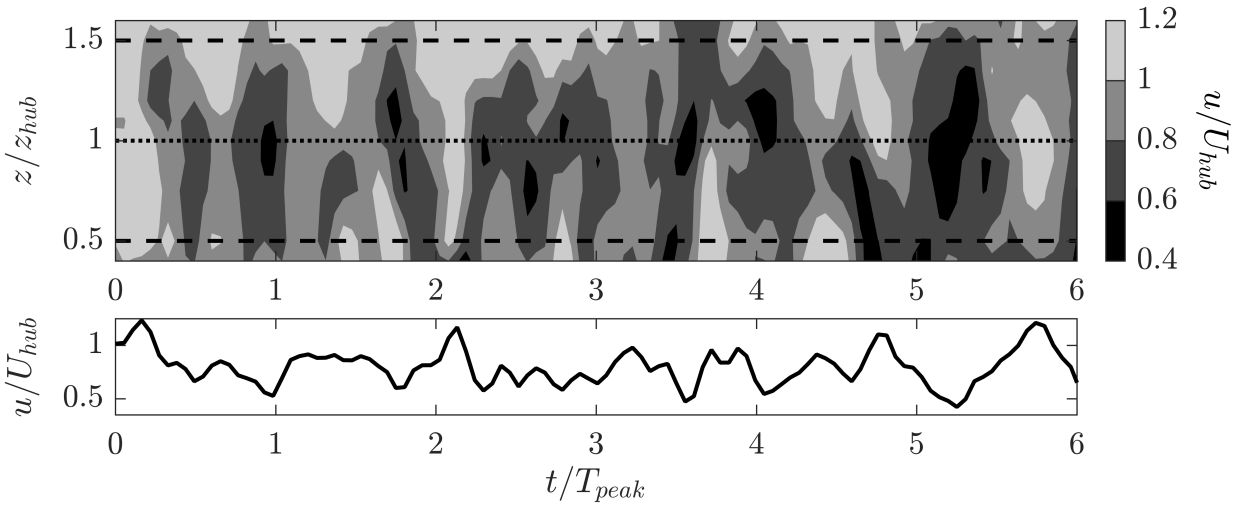

Figure 7. A sample spatio-temporal streamwise velocity signal using the wake measurements of field deployment 4. The velocity contour (top) represents the vertical profile in time. Horizontal lines indicate the turbine hub height (dotted) and tip heights (dashed). The velocity signal in the bottom figure is for the hub height streamwise velocity. The 4-minute time series is normalized by the period of the meandering spectral peak $T_{peak} = 1/f_{peak} \approx 40$ s.

regions appear to be well-centered with the turbine hub height and vertically coincide with the tip-height limits of the rotor. The deficit pattern is indicative of a wake oscillating transversely and periodically aligning with the WindCube north and south LOS. The observed variability of the wake oscillations in Figure 7 – likely an effect of variability in the inflow conditions – manifests in the pre-multiplied spectra as the broad excess energy range $St = 0.1$–0.7 seen in Figure 6 as opposed to a sharp peak. These Strouhal range limits correspond to time periods of 116 s and 17 s, respectively.

4.3. Wake energy deficit

Figure 8 shows the large-scale energy deficit centroid for the wind tunnel spectra and the two field spectra with clear energy deficits. The Φ value of the centroid is normalized by the inflow Φ at the same frequency $St_{centroid}$. The error bars in the figure represent the average difference between the plotted centroid and the centroids calculated using the lower and upper correction uncertainty bounds, i.e. the dashed lines in Figure 6.

The level of energy deficit is comparable between the wind tunnel and field spectra. The Strouhal number is higher for the field data, but using longer spectrum windows would introduce longer time scales that would reduce the centroid Strouhal number. In both the wind tunnel and field spectra, the upper Strouhal limit of the energy deficit is in the range $St = 0.06 - 0.1$. The observed consistency of the upper Strouhal limit may be partly insured by the scaling of the wind

DOI: 10.1002/we

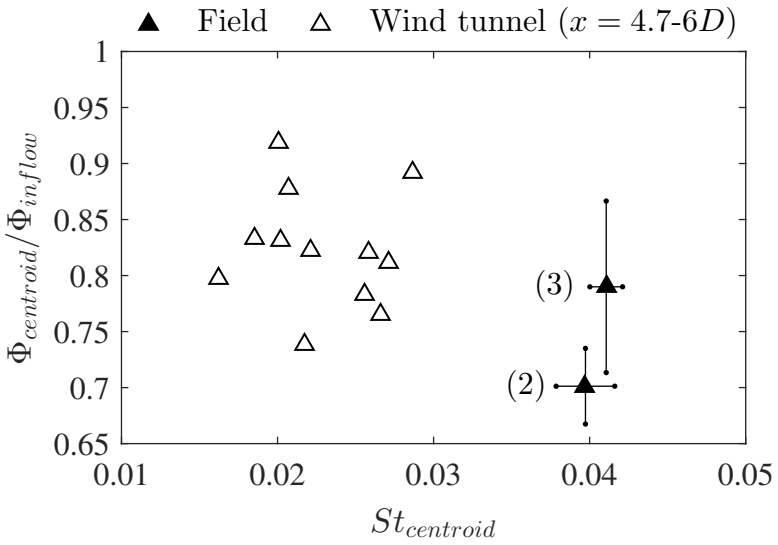

Figure 8. Comparison of amplitude and Strouhal number for the centroid of large-scale energy deficit in the wake spectra. The number labels correspond to the field deployments in Table I. Field deployments 1, 4, and 5 are not included; field deployments 1 and 4 have no Φ_{inflow} for scaling the amplitude, and field deployment 5 exhibited no energy deficit.

tunnel model turbine. The model turbine hub height and rotor diameter are scaled such that the rotor occupies the same region of the wind tunnel boundary layer as utility-scale turbines in the atmospheric boundary layer.

At the field scale, the $St = 0.06$–0.1 Strouhal range corresponds to time scales of approximately 3 minutes and length scales of 1500 m, or 5δ for a nominal boundary layer height of 300 m. These scales are of the same order of magnitude as the very large scale motions and superstructures populating the canonical turbulent boundary layer [47, 48, 43, 49]. The large-scale energy deficit in the findings is interpreted as a sheltering effect of the turbine. The rotor area partially disrupts or deflects the largest flow scales (> 3 minutes at the field scale), reducing their contribution to the overall energy in the wake. Note that the energy transfer mechanism from very large to smaller scales is highly dissipative and inferred to reduce the inhomogeneities and asymmetry of the incoming boundary layer turbulence, promoting the homogenization of the wake [50, 51].

4.4. Wake energy excess

Figure 9 shows the turbulent wake energy excess peak and centroid for the wind tunnel spectra and the three field spectra with available inflow conditions. The Φ_u value of the centroid and peak is normalized by the inflow Φ_{inflow} at the same frequency St. The error bars represent the uncertainty bounds as in Figure 8. The excess energy centroid for deployment

DOI: 10.1002/we

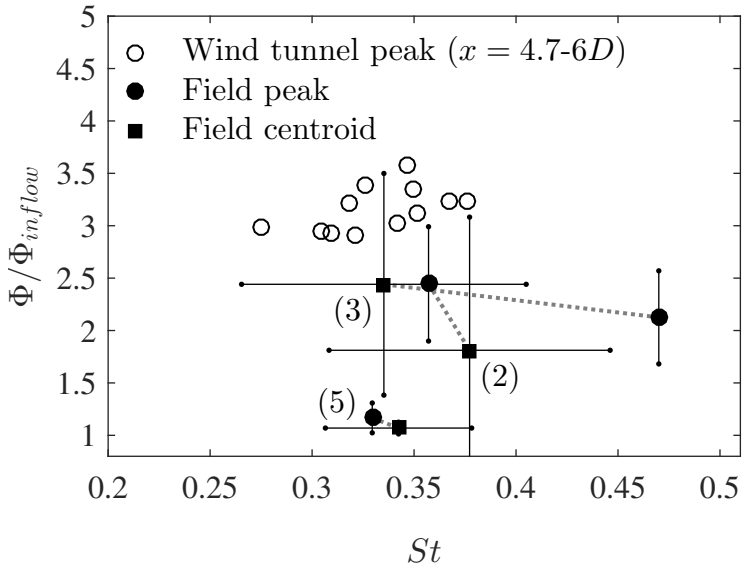

Figure 9. Comparison of amplitude and Strouhal number for excess energy in the wake spectra. The wake excess energy is represented by two methods: the peak in the pre-multiplied spectrum $(St_{peak}, \Phi_{peak}/\Phi_{inflow})$ and the centroid of excess energy in the spectrum $(St_{centroid}, \Phi_{centroid}/\Phi_{inflow})$. The field-scale peaks and centroids are indicated in Figure 6. Dotted lines connect the corresponding peak and centroid for a given deployment. The number labels correspond to the field deployments in Table I with turbine performances (2) $C_p = 0.43$, (3) $C_p = 0.40$, and (5) $C_p = 0.19$. Field deployments 1 and 4, having no Φ_{inflow} for scaling the amplitude, are not included.

3 is more consistent with both the other field deployment data points and wind tunnel peaks, indicating the centroid is a more robust way to represent the clustering of excess wake meandering kinetic energy in the field data.

While the laboratory inflow conditions were observed to provide a genuine, scaled representation of the atmospheric surface layer at the Eolos site [33, 14, 52], the model and utility-scale turbine performances are significantly different. In particular, the wake deficit in the miniature turbine models is due to a relatively large drag as opposed to an efficient energy harnessing (see discussion in [52]). It is thus speculated here that the wake energy excess is primarily associated with the tip vortex structure and annular shear layer delimiting the rotor wake: a high performing field-scale turbine with optimal blade design would ensure high shear, large deficit, and a strong meandering wake (deployments 2, 3, 4); the same turbine in a derated state would have a weaker tip vortex structure, shear layer, mean deficit, and meandering wake (deployment 5). A sub-optimal turbine model, as in wind tunnel studies, sustains large wake oscillations through high shear and large velocity deficit induced by high drag. As a further confirmation, actuator disk models generate high drag without producing mechanical energy and are able to generate a meandering wake [35, 54].

DOI: 10.1002/we

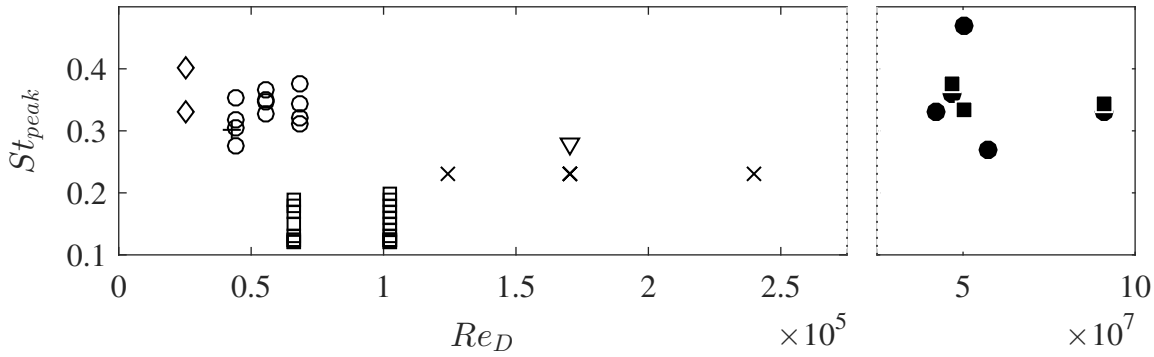

Figure 10. Comparison of Strouhal number for peaks in the wake pre-multiplied spectra with experimental Reynolds number $Re_D = DU_{hub}/\nu$. The plot includes results of the current lab ($\circ$) and field (peaks $\bullet$, centroids $\blacksquare$) experiments and the following literature: Medici 2006 ($\square$) [22], Chamorro 2010 ($\diamond$) [31], Chamorro 2013 ($\triangledown$) [32], Okulov 2014 ($\times$) [27], and Howard 2015 ($+$) [33].

The Strouhal numbers of the wind tunnel pre-multiplied peaks and field excess energy centroids are consistent with previous literature [22, 31, 32, 27, 33]. Figure 10 shows the pre-multiplied peak Strouhal number versus the turbine diameter Reynolds number for the current experiment results and published literature. The literature data points were interpreted from plotted and stated results in the referenced material. The meandering frequency maintains the same range of Strouhal number as in the laboratory scale, and is thus inferred to be independent of the Reynolds number. The wake meandering oscillations prove to be a robust feature of turbine wakes under the investigated range of inflow and operating conditions including variability in thermal stability and turbine siting.

We acknowledge the range of St_{peak} in Figure 10 may be partly explained by the strength of the shear layer through the operating conditions [23] as discussed above. However, the effect of the operating conditions is more explicitly seen in the amplitude of excess energy (see Figure 9). Considering four orders of magnitude in turbine diameter D are represented in Figure 10, the meandering frequency is only weakly affected by operating conditions and is unambiguously governed by the rotor shear scaling U_{hub}/D which normalizes the Strouhal number.

5. DISCUSSION: THE TWO SCALES OF WAKE MEANDERING

We posit here the presence of wake turbulence effects at two separate scales, individually driven by the two mechanisms discussed in the literature. The first, designated as dynamic wake meandering, is the redirection of the wake as it is convected by the incoming flow [24]. The second is (relatively) small-scale periodic meandering of the wake due to instability of the annular shear layer [22], consistent with bluff body wakes.

DOI: 10.1002/we

For the incoming flow mechanism, very large-scale motions steer the direction of the wake for long time scales as has been shown in [29, 30]. The dynamic wake meandering model is thereby able to accurately predict wake position for time scales comparable to those of the largest scale structures of the incoming flow. These scales correspond to a deficit of low-frequency turbulent energy in the wake velocity spectrum. The interaction of the incoming flow and the turbulent wake structure occurs at the shear layer surrounding the rotor and is marked by strong local velocity gradients. In the near wake, the shear contributes to break the tip vortex structure, resulting in vortex breakdown and vortex interaction mechanisms [16] characterized by intense dissipation of turbulent kinetic energy. Thus, along the turbine wake the kinetic energy of the incoming flow is transferred from large to small scales, leading to the low-frequency energy deficit seen in [25, 32] and here in Figure 8 for both lab and field scales. While the characteristic size of the largest scales is dependent on incoming flow parameters such as boundary layer height and thermal stability, the smallest scale experiencing an energy deficit in the wake is dictated by the turbine rotor geometry [32], leading to a collapse of the energy deficit upper limit when scaled as the Strouhal number. The upper limit of the energy deficit in the present study consistently corresponds to length scales $10D$–$15D$, which is inferred to mark the lower range of the scales relevant to dynamic wake meandering. While incoming flow scales smaller than $10D$–$15D$ are unimpeded by the turbine, larger scales contribute to the location and steering of the wake and appear dampened downwind of the turbine.

Separately, the rotor shear instability mechanism is supported by the excess in turbulent wake energy seen in Figure 9 and previous findings [22, 31, 32, 27, 33]. Rotor shear instability effects scale in size with the turbine diameter and are relatively small compared to the largest scales of motion in the boundary layer. Recent works have identified various dynamics as being responsible for the onset of turbine wake meandering: the mutual interaction of individual tip vortices, observed under uniform inflow conditions [27]; and the interaction of the radially expanding hub vortex with the outer shear layer, observed for hydrokinetic turbines [35] and a model wind turbine [33]. For each case, meandering initiates when the unstable annular shear layer separating the low-momentum wake from the high-momentum free stream flow is sufficiently disrupted following the collapse or break-up of the tip vortex structure, leading to mixing and entrainment of the free stream flow into the wake and eventual wake recovery [35]. The exact mechanism for initiating meandering is yet unknown for utility-scale wind turbines. The onset may involve ambient turbulence which has been shown to break up tip vortices for utility-scale turbines [53], and may not involve the hub vortex because, unlike for model wind and hydrokinetic turbines, the nacelle diameter is significantly smaller relative to the rotor diameter.

While the onset of meandering is likely dependent on turbine design and flow scale, the meandering frequency is not. The frequency is dictated by rotor scaling as the Strouhal number and is independent of Reynolds number as shown in

DOI: 10.1002/we

Figure 10. The amount of wake energy added appears to depend on contributions of both the drag and turbine performance to the strength of the shear layer [55]. At the field scale, the shear instability meandering period ($\sim$ 30 s) is shorter than the large time scales of the the incoming flow and does not dictate the wake position over extended time periods. However, whereas the wake is somewhat sheltered from large-scale energy by the turbine, shear instability meandering increases energy within the envelope of the wake, adding turbulent energy to a specific frequency range. In a simplified practical sense, the large scales of the incoming flow contribute to whether a turbine in a wind farm is positioned in the wake of an upstream turbine (dynamic wake meandering), whereas the wake shear instability determines the frequency and amplitude of added turbulent energy that the downstream turbine will experience (rotor shear wake meandering).

6. CONCLUSIONS

The experiments presented in this study of turbine wakes were executed across a range of parameter spaces: at the laboratory scale in an atmospheric wind tunnel under controlled steady conditions; at a topographically flat field site with canonical rough wall inflow conditions; in a wind farm with a turbine likely undergoing complex inflow conditions due to upstream turbines; for turbines performing optimally and sub-optimally with respect to the power coefficient and tip-speed ratio; and at various downstream wake positions ranging $2D$–$6D$. While inherent limitations exist in the turbulence measurements of the ground-based LiDAR, two persistent trends beyond the experimental uncertainty emerge from the streamwise hub height velocity spectra.

First, a deficit occurs in the large-scale turbulent energy. The deficit upper limit appears invariant in the Strouhal number under varying Reynolds number. This observation suggests i) the importance of large scale structures in the atmospheric boundary layer which impinge on the turbine rotor and are deflected or destroyed in the wake; ii) a sheltering effects by the turbine that may propagate to reduce near surface fluxes in the turbine wake.

Second, excess turbulent energy is seen for field experiments with the central frequency (identified as the excess energy peak or centroid) in the Strouhal number range $St = fD/U_{hub} = 0.3$–0.4, consistent with wake meandering observed in the wind tunnel and reported in the literature. The invariance of the spectral signature location under varying rotor-diameter-based Reynolds number over three orders of magnitude unequivocally confirms the importance of the rotor shear scaling with U_{hub}/D in the normalization of the wake meandering frequency, leading to the Strouhal number.

The excess energy findings emphasize the importance of vortex shedding mechanisms by the rotor in destabilizing the turbine wake at relatively short time scales. At the same time, the observed energy deficit is consistent with previous experiments showing the incoming large scales of turbulence to steer the wake at relatively larger time scales [29, 30]. The

DOI: 10.1002/we

large-scale deficit and meandering frequency are both contingent upon turbine performance, which dictates the strength of the tip vortex structure and annular shear layer. The field experimental case with the highly derated turbine ($C_p = 0.19$) exhibited neither deficit nor a distinct meandering signature. The low power coefficient and small velocity deficit resulted in a weaker mean shear across the rotor and a dampening of meandering. Also, measurements at field scale at $1.8D$ did not show any wake meandering, suggesting the onset is spatially delayed as compared to the miniature wind turbines [33].

A. APPENDIX: WIND TUNNEL MEASUREMENTS

Model turbine wake measurements were collected in the St Anthony Falls Laboratory closed-loop atmospheric boundary layer wind tunnel for comparison with field-scale results. The tunnel test section length is 16 m and the cross section is 1.7 m $\times$ 1.7 m. A turbulence trip at the test section leading edge develops a boundary layer under zero pressure gradient conditions, keeping the turbine hub height z_{hub} in the bottom 25% of the boundary layer height $\delta \approx 0.6$ m (see [56, 31, 14, 52] for example boundary layer and wake profiles). The free stream and floor surface temperatures can be controlled to simulate different thermal stability conditions. Neutral thermal conditions were employed for the experiments in this study. The model wind turbine used in the wind tunnel experiments has a three-blade GWS/EP-5030x3 rotor with a 0.128 m rotor diameter and 0.104 m hub height [56, 50, 33, 52]. The optimal tip-speed ratio of the model is $\lambda \approx 3.2$. For similar wind tunnel experiments see [57].

Streamwise and spanwise velocity components u and v were measured with a Dantec cross hot-wire probe connected to an A.A. Lab anemometer system. The anemometer system was calibrated using a separate temperature-controlled calibration box with laminar flow output. The probe was positioned in different downstream distances at the model turbine hub height using a traverse system. For each run, data were acquired at 20 kHz for 180 s. The experiment consisted of measurements at four downstream distance ($4.7D$, $5.1D$, $5.5D$, and $6D$) and three free stream hub-height velocities (5 m s^{-1}, 6.25 m s^{-1}, and 7.5 m s^{-1}), totaling twelve cases. The tip-speed ratio was maintained at $\lambda \approx 5$ for each case. The rotor diameter Reynolds number $Re_D = U_{hub}D/\nu$ was of the order $Re_D \sim O(10^4)$, while for the field-scale deployments the Reynolds number was of the order $Re_D \sim O(10^7)$.

The key differences between the model turbine geometry and the utility-scale turbines are i) the blade geometry and aerodynamics, associated with a much smaller chord-based Reynolds number, ii) the absence of variable torque, pitch and the related control algorithm, and iii) the ratio of the rotor to nacelle hub diameters. These differences are responsible for the lower power coefficient and operational tip-speed ratio of the model turbine (see [14]). Along with the effect of larger separation of scales in the incoming flow, the geometric differences may also result in a different flow structure in the wake

DOI: 10.1002/we

and a different mechanism for the onset of wake meandering. For these reasons we compare results at both laboratory and field scales.

B. APPENDIX: LIDAR SPECTRAL CORRECTION

For the current study, an empirical velocity spectrum correction was created for each deployment featuring LiDAR wake measurements. The correction for the overestimated turbulent energy in the inertial sub-range [40, 17, 19] uses historical LiDAR and sonic anemometer data to predict and compensate the overestimation. Since the analysis in the study compared LiDAR wake spectra to sonic anemometer inflow spectra, the corrections are relative to the sonic results, i.e. it is assumed the estimated sonic spectra are representative. The assumption is valid for the specific frequency range of interest.

B.1. Baseline data

In 2012, the WindCube was positioned at the Eolos met tower to capture velocity measurements continuously for approximately 200 days. Under these conditions the Windcube and met tower sonic anemometer measurements should theoretically be equal, with any discrepancies in velocity measurements due to measurement uncertainty and limitations (e.g. sampling volume and frequency). For each field deployment, the 200 days of data were assessed to select baseline periods where the conditions were similar to the deployment. By matching the boundary conditions, the underlying cause of the LiDAR variance overestimation is assumed to be similar such that the error in measured variance is also similar. The five criteria below were used in selecting baseline periods, where the last two criteria are of secondary importance:

1. The period was one hour or longer to allow for sufficient averaging of the windowed velocity spectrum.
2. The wind direction was along a LiDAR LOS ($\pm 15^{\circ}$) to allow for accurate streamwise velocity calculations using two radial velocity measurements as in equation (1). The considered wind direction range was also limited to exclude periods where the wind direction was outside the sonic anemometer limits ($\pm 120^{\circ}$ from the sonic orientation) and periods when the met tower or any LiDAR LOS was in the turbine wake.
3. The mean wind magnitude was comparable to the deployment ($\pm 20\%$) with small variations in the mean conditions.
4. The time of day (i.e. daytime versus nighttime) was the same as the deployment to match the phase of the diurnal thermal stability cycle.
5. The time of year was the same as the deployment to match the surface roughness of the field site. The roughness changes through the year due to factors including crop growth and snow cover.

DOI: 10.1002/we

The criteria were purposefully subjective to allow for manual selection of periods rather than algorithmic. Eight or more baseline periods were selected for each deployment using the above criteria (the minimum number of baselines was not dictated).

B.2. Shape correction

For each baseline period of a given field deployment, the shape correction factor was estimated as the difference between the LiDAR and sonic spectra in the baseline period: $C_u(f) = \Phi_{sonic}/\Phi_{LiDAR}$. Outlier baseline periods were manually identified and excluded by viewing the collective correction factors $C_u(f)$. The final shape correction for the deployment is the average of the correction factors, and the correction uncertainty is represented as the standard deviation of the correction factors. The mean and standard deviation were weighted by the baseline period length to favor longer periods. Figure 11 provides an example of the empirical correction applied to deployment 5. Figure 11(a) shows the LiDAR and sonic velocity spectra for a baseline period in October 2012. The energy overestimation occurs in the frequency range 0.02 Hz to 0.1 Hz. Figure 11(b) shows the shape correction factor for all baseline periods along with the weighted mean and standard deviation. The mean correction factor is 1 (i.e. no correction) for low frequencies, and reaches a minimum $C_u = 0.6$ at $f = 0.06$ Hz corresponding to a 67% overestimation. The largest correction variability occurs around $f = 0.02$ Hz, the beginning of the overestimated range. However, the correction variability is small where the overestimation is largest. This in particular has positive implications, since the variability in the correction factor contributes to the experimental uncertainty and uncertainty in detection of spectral signatures (shown as uncertainty bounds in Figure 6 and error bars in Figures 8 and 9).

The corrected spectrum is eventually calculated from the final correction factor as $\Phi_{corrected} = C_u\Phi_{uncorrected}$. Figures 11(c) and 11(d) show the correction mean and standard deviation applied to the wake deployment 5 spectrum and pre-multiplied spectrum, respectively. The effect of the wake turbulence on the energy spectrum is given by the discrepancy between the inflow and wake spectra after the correction has been applied. In this case the excess energy is accounted for entirely by the overestimation. Spectra plots of the field measurements in the main paper follow the format of Figure 11(d) without showing the uncorrected wake spectrum.

ACKNOWLEDGEMENTS

The authors acknowledge funding support from the Institute on the Environment (IonE), the National Science Foundation (Grant: 1351303, PI: M. Guala), and the University of Minnesota Civil, Environmental, and Geo- Engineering Department,

DOI: 10.1002/we

Prepared using weauth.cls

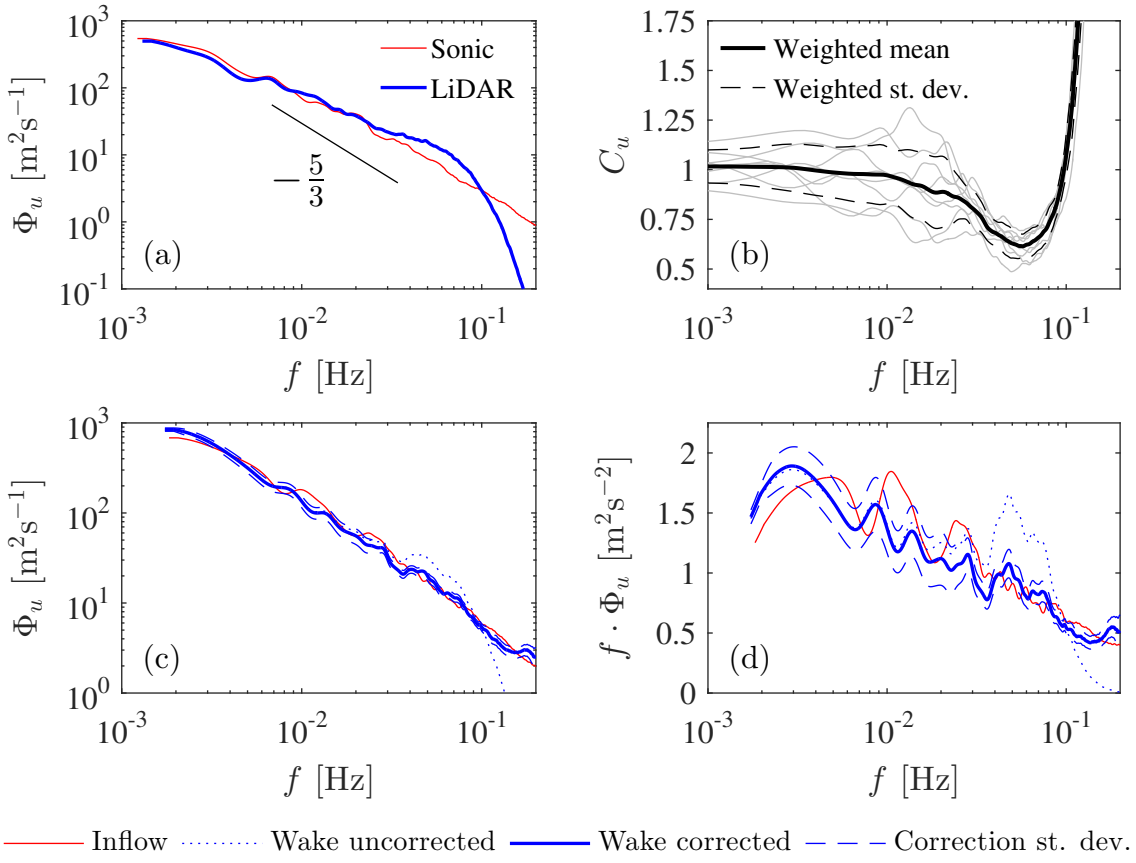

Figure 11. Demonstration of the empirical correction to LiDAR one-dimensional velocity spectra estimates: (a) sonic anemometer and LiDAR spectra for baseline measurements where the spectra should theoretically be equal; (b) LiDAR spectrum shape correction $C_u(f) = \Phi_{sonic}/\Phi_{LiDAR}$ for several baseline periods, with the correction mean and standard deviation weighted by the baseline period durations; (c) the correction mean and standard deviation applied to a LiDAR wake spectrum where $\Phi_{corrected} = C_u\Phi_{uncorrected}$; (d) the spectra of plot (c) pre-multiplied. The bottom legend corresponds to plots (c) and (d).

in addition to Mirko Musa, Christopher Feist, Christopher Milliren, and Xcel Energy for their assistance and cooperation with field deployments.

REFERENCES

1. Clifton A, Schreck S, Scott G, Kelley N, Lundquist JK. Turbine Inflow Characterization at the National Wind Technology Center. *Journal of Solar Energy Engineering*, 135(3):031017, 2013, DOI: 10.1115/1.4024068.
2. Clifton A, Daniels MH, Lehning M. Effect of winds in a mountain pass on turbine performance. *Wind Energy*, 17(10):1543–1562, 2014, DOI: 10.1002/we.1650.

3. Chamorro LP, Lee SJ, Olsen D, Milliren C, Marr J, Arndt REA, Sotiropoulos F. Turbulence effects on a full-scale 2.5 MW horizontal-axis wind turbine under neutrally stratified conditions. *Wind Energy*, 18(2):339–349, 2015, DOI: 10.1002/we.1700.
4. Kelley CL, Ennis BL. SWiFT site atmospheric characterization. Technical report, Sandia National Laboratories (SNL), Albuquerque, NM, and Livermore, CA (United States), 2016, DOI: 10.2172/1237403.
5. Wagner R, Pedersen TF, Courtney M, Antoniou I, Davoust S, Rivera RL. Power curve measurement with a nacelle mounted lidar. *Wind Energy*, 17(9):1441–1453, 2014, DOI: 10.1002/we.1643.
6. Aitken ML, Lundquist, JK. Utility-Scale Wind Turbine Wake Characterization Using Nacelle-Based Long-Range Scanning Lidar. *Journal of Atmospheric and Oceanic Technology*, 31(7):1529–1539, 2014, DOI: 10.1175/JTECH-D-13-00218.1.
7. Machefaux E, Larsen GC, Troldborg N, Hansen KS, Angelou N, Mikkelsen T, Mann J. Investigation of wake interaction using full-scale lidar measurements and large eddy simulation. *Wind Energy*, 19(8):1535–1551, 2016, DOI: 10.1002/we.1936.
8. Machefaux E, Larsen GC, Koblitz T, Troldborg N, Kelly MC, Chougule A, Hansen KS, and Rodrigo JS. An experimental and numerical study of the atmospheric stability impact on wind turbine wakes. *Wind Energy*, 19(10):1785–1805, 2016, DOI: 10.1002/we.1950.
9. Banta RM, Pichugina YL, Kelley ND, Hardesty RM, Brewer WA. Wind Energy Meteorology: Insight into Wind Properties in the Turbine-Rotor Layer of the Atmosphere from High-Resolution Doppler Lidar. *Bulletin of the American Meteorological Society*, 94(6):883–902, 2013, DOI: 10.1175/BAMS-D-11-00057.1.
10. Rhodes ME, Lundquist JK. The Effect of Wind-Turbine Wakes on Summertime US Midwest Atmospheric Wind Profiles as Observed with Ground-Based Doppler Lidar. *Boundary-Layer Meteorology*, 149(1):85–103, 2013, DOI: 10.1007/s10546-013-9834-x.
11. Iungo GV, Wu YT, Porté-Agel F. Field measurements of wind turbine wakes with lidars. *Journal of Atmospheric and Oceanic Technology*, 30(2):274–287, 2013, DOI: 10.1175/JTECH-D-12-00051.1.
12. Iungo GV, Porté-Agel F. Measurement procedures for characterization of wind turbine wakes with scanning Doppler wind LiDARs. *Advances in Science and Research*, 10:71, 2013, DOI: 10.5194/asr-10-71-2013.
13. Trabucchi D, Steinfeld G, Bastine D, Trujillo JJ, Schneemann J, Kühn M. Study of wake meandering by means of fixed point lidar measurements: Spectral analysis of line-of-sight wind component. *Journal of Physics: Conference Series*, 625:012016, 2015, DOI: 10.1088/1742-6596/625/1/012016.

14. Howard KB, Guala M. Upwind preview to a horizontal axis wind turbine: a wind tunnel and field-scale study. *Wind Energy*, 19(8):1371–1389, 2016, DOI: 10.1002/we.1901.

15. Toloui M, Riley S, Hong J, Howard KB, Chamorro LP, Guala M, Tucker J. Measurement of atmospheric boundary layer based on super-large-scale particle image velocimetry using natural snowfall. *Experiments in Fluids*, 55(5):1737, 2014, DOI: 10.1007/s00348-014-1737-1.

16. Hong J, Toloui M, Chamorro LP, Guala M, Howard KB. Natural snowfall reveals large-scale flow structures in the wake of a 2.5-MW wind turbine. *Nature communications*, 5, 2014, DOI: 10.1038/ncomms5216.

17. Sathe A, Mann J. Measurement of turbulence spectra using scanning pulsed wind lidars. *Journal of Geophysical Research*, 117(D1), 2012, DOI: 10.1029/2011JD016786.

18. Sathe A, Mann J. A review of turbulence measurements using ground-based wind lidars. *Atmospheric Measurement Techniques*, 6(11):3147–3167, 2013, DOI: 10.5194/amt-6-3147-2013.

19. Newman JF, Klein PM, Wharton S, Sathe A, Bonin TA, Chilson PB, Muschinski A. Evaluation of three lidar scanning strategies for turbulence measurements. *Atmospheric Measurement Techniques*, 9(5):1993–2013, 2016, DOI: 10.5194/amt-9-1993-2016.

20. Wang H, Barthelmie RJ, Doubrawa P, Pryor SC. Errors in radial velocity variance from Doppler wind lidar. *Atmospheric Measurement Techniques*, 9(8):4123–4139, 2016, DOI: 10.5194/amt-9-4123-2016.

21. Vermeer LJ, Sørensen JN, Crespo A. Wind turbine wake aerodynamics. *Progress in Aerospace Sciences*, 39(6-7):467–510, 2003, DOI: 10.1016/S0376-0421(03)00078-2.

22. Medici D, Alfredsson PH. Measurements on a wind turbine wake: 3D effects and bluff body vortex shedding. *Wind Energy*, 9(3):219–236, 2006, DOI: 10.1002/we.156.

23. Medici D, Alfredsson PH. Measurements behind model wind turbines: further evidence of wake meandering. *Wind Energy*, 11(2):211–217, 2008, DOI: 10.1002/we.247.

24. Larsen GC, Madsen HA, Thomsen K, Larsen TJ. Wake meandering: a pragmatic approach. *Wind Energy*, 11(4):377–395, 2008, DOI: 10.1002/we.267.

25. España G, Aubrun S, Loyer S, Devinant P. Wind tunnel study of the wake meandering downstream of a modelled wind turbine as an effect of large scale turbulent eddies. *Journal of Wind Engineering and Industrial Aerodynamics*, 101:24–33, 2012, DOI: 10.1016/j.jweia.2011.10.011.

26. Iungo GV, Viola F, Camarri S, Porté-Agel F, Gallaire F. Linear stability analysis of wind turbine wakes performed on wind tunnel measurements. *Journal of Fluid Mechanics*, 737:499–526, 2013, 10.1017/jfm.2013.569.

27. Okulov VL, Naumov IV, Mikkelsen RF, Kabardin IK, Sørensen JN. A regular Strouhal number for large-scale instability in the far wake of a rotor. *Journal of Fluid Mechanics*, 747(2014):369–380, 2014, DOI: 10.1017/jfm.2014.174.

28. Stevens R, Meneveau C. Flow Structure and Turbulence in Wind Farms. *Annual Review of Fluid Mechanics*, 49(1):311–339, 2017, DOI: 10.1146/annurev-fluid-010816-060206.

29. Bingöl F, Mann J, Larsen GC. Light detection and ranging measurements of wake dynamics part I: one-dimensional scanning. *Wind Energy*, 13(1):51–61, 2010, DOI: 10.1002/we.352.

30. Trujillo JJ, Bingöl F, Larsen GC, Mann J, Kühn M. Light detection and ranging measurements of wake dynamics. Part II: two-dimensional scanning. *Wind Energy*, 14(1):61–75, 2011, DOI: 10.1002/we.402.

31. Chamorro LP, Porté-Agel F. Effects of Thermal Stability and Incoming Boundary-Layer Flow Characteristics on Wind-Turbine Wakes: A Wind-Tunnel Study. *Boundary-Layer Meteorology*, 136(3):515–533, 2010, DOI: 10.1007/s10546-010-9512-1.

32. Chamorro LP, Hill C, Morton S, Ellis C, Arndt REA, Sotiropoulos F. On the interaction between a turbulent open channel flow and an axial-flow turbine. *Journal of Fluid Mechanics*, 716:658–670, 2013, DOI: 10.1017/jfm.2012.571.

33. Howard KB, Singh A, Sotiropoulos F, Guala M. On the statistics of wind turbine wake meandering: An experimental investigation. *Physics of Fluids*, 27(7):075103, 2015, DOI: 10.1063/1.4923334.

34. Foti D, Yang X, Guala M, Sotiropoulos F. Wake meandering statistics of a model wind turbine: Insights gained by large eddy simulations. *Physical Review Fluids*, 1(4):044407, 2016, DOI: 10.1103/PhysRevFluids.1.044407.

35. Kang S, Yang X, Sotiropoulos F. On the onset of wake meandering for an axial flow turbine in a turbulent open channel flow. *Journal of Fluid Mechanics*, 744:376–403, 2014, DOI: 10.1017/jfm.2014.82.

36. Portfolio, RES - Global Renewable Energy Company. www.res-group.com/en/portfolio/?ProjectID=2018. Accessed July 2017.

37. Vestas. V100-2.0 MW Wind Turbine. www.vestas.com/en/products/turbines/v100%202_0_mw. Accessed July 2017.

38. Anderson Jr, JD. Fundamentals of aerodynamics (6th edition). *McGraw-Hill Education*, 2017.

39. Courtney M, Wagner R, Lindelöw P. Testing and comparison of lidars for profile and turbulence measurements in wind energy. *IOP Conference Series: Earth and Environmental Science*, 1:012021, 2008, DOI: 10.1088/1755-1315/1/1/012021.

40. Canadillas B, Bégué A, Neumann T. Comparison of turbulence spectra derived from LiDAR and sonic measurements at the offshore platform FINO1. In *10th German Wind Energy Conference (DEWEK 2010)*, pages 18–21, 2010.

41. Toloui M, Chamorro LP, Hong J. Detection of tip-vortex signatures behind a 2.5 MW wind turbine. *Journal of Wind Engineering and Industrial Aerodynamics*, 143:105–112, 2015, DOI: 10.1016/j.jweia.2015.05.001.

42. Jiménez A, Crespo A, Migoya E. Application of a LES technique to characterize the wake deflection of a wind turbine in yaw. *Wind Energy*, 13(December 2009):559–572, 2010, DOI: 10.1002/we.380.

43. Guala M, Metzger M, McKeon BJ. Interactions within the turbulent boundary layer at high Reynolds number. *Journal of Fluid Mechanics*, 666:573–604, 2011, DOI: 10.1017/S0022112010004544.

44. Chamorro LP, Guala M, Arndt REA, Sotiropoulos F. On the evolution of turbulent scales in the wake of a wind turbine model. *Journal of Turbulence*, 13:N27, 2012, DOI: 10.1080/14685248.2012.697169.

45. Kaimal JC, Wyngaard JC, Izumi Y, Coté OR. Spectral characteristics of surface-layer turbulence. *Quarterly Journal of the Royal Meteorological Society*, 98(417):563–589, 1972, DOI: 10.1002/qj.49709841707.

46. Foti D. *Quantification and reduction of uncertainty of model predictions of wind turbines and plants via high-fidelity simulations*. PhD thesis, University of Minnesota, 2016.

47. Balakumar BJ, Adrian RJ. Large- and very-large-scale motions in channel and boundary-layer flows. *Philosophical Transactions of the Royal Society A: Mathematical, Physical and Engineering Sciences*, 365(1852):665–681, 2007, DOI: 10.1098/rsta.2006.1940.

48. Hutchins N, Marusic I. Evidence of very long meandering features in the logarithmic region of turbulent boundary layers. *Journal of Fluid Mechanics*, 579:1, 2007, DOI: 10.1017/S0022112006003946.

49. Smits AJ, McKeon BJ, Marusic I. High–Reynolds Number Wall Turbulence. *Annual Review of Fluid Mechanics*, 43(1):353–375, 2011, DOI: 10.1146/annurev-fluid-122109-160753.

50. Singh A, Howard KB, Guala M. On the homogenization of turbulent flow structures in the wake of a model wind turbine. *Physics of Fluids*, 26(2):025103, 2014, DOI: 10.1063/1.4863983.

51. Singh A, Howard KB, Guala M. A measure of scale-dependent asymmetry in turbulent boundary layer flows: scaling and Reynolds number similarity. *Journal of Fluid Mechanics*, 797(2):549–563, 2016, DOI: 10.1017/jfm.2016.294.

52. Howard KB, Chamorro LP, Guala M. A Comparative Analysis on the Response of a Wind-Turbine Model to Atmospheric and Terrain Effects. *Boundary-Layer Meteorology*, 158(2):229–255, 2016, DOI: 10.1007/s10546-015-0094-9.

53. Yang X, Hong J, Barone M, Sotiropoulos F. Coherent dynamics in the rotor tip shear layer of utility-scale wind turbines. *Journal of Fluid Mechanics*, 804:90–115, 2016, DOI: 10.1017/jfm.2016.503.

54. Sørensen JN. Aerodynamic Aspects of Wind Energy Conversion. *Annual Review of Fluid Mechanics*, 43(1):427–448, 2011, DOI: 10.1146/annurev-fluid-122109-160801.

55. Annoni J, Howard KB, Seiler P, Guala M. An experimental investigation on the effect of individual turbine control on wind farm dynamics. *Wind Energy*, 19(8):1453–1467, 2015, DOI: 10.1002/we.1930.

56. Chamorro LP, Porté-Agel F. A Wind-Tunnel Investigation of Wind-Turbine Wakes: Boundary-Layer Turbulence Effects. *Boundary-Layer Meteorology*, 132(1):129–149, 2009, DOI: 10.1007/s10546-009-9380-8.

57. Cal RB, Lebrón J, Castillo L, Kang HS, Meneveau C. Experimental study of the horizontally averaged flow structure in a model wind-turbine array boundary layer. *Journal of Renewable and Sustainable Energy*, 2(1):013106, 2010, DOI: 10.1063/1.3289735.